

All sky CMB map from cosmic strings integrated Sachs-Wolfe effect

Christophe Ringeval*

*Centre for Cosmology, Particle Physics and Phenomenology, Institute of Mathematics and Physics,
Louvain University, 2 Chemin du Cyclotron, 1348 Louvain-la-Neuve, Belgium*

François R. Bouchet†

Institut d'Astrophysique de Paris, UMR CNRS 7095, Université Pierre et Marie Curie, 98bis boulevard Arago, 75014 Paris, France

(Received 23 April 2012; published 9 July 2012)

By actively distorting the cosmic microwave background (CMB) over our past light cone, cosmic strings are unavoidable sources of non-Gaussianity. Developing optimal estimators able to disambiguate a string signal from the primordial type of non-Gaussianity requires calibration over synthetic full sky CMB maps, which until now had been numerically unachievable at the resolution of modern experiments. In this paper, we provide the first high resolution full sky CMB map of the temperature anisotropies induced by a network of cosmic strings since the recombination. The map has about 200 million subarcminute pixels in the healpix format which is the standard in use for CMB analyses ($N_{\text{side}} = 4096$). This premiere required about 800 000 cpu-hours; it has been generated by using a massively parallel ray tracing method piercing through thousands of state of art Nambu-Goto cosmic string numerical simulations which pave the comoving volume between the observer and the last scattering surface. We explicitly show how this map corrects previous results derived in the flat sky approximation, while remaining completely compatible at the smallest scales.

DOI: [10.1103/PhysRevD.86.023513](https://doi.org/10.1103/PhysRevD.86.023513)

PACS numbers: 98.80.Cq, 98.70.Vc

I. INTRODUCTION

As all topological defects [1], cosmic strings incessantly generate gravitational perturbations all along the history of the Universe [2–4]. Their amplitude is directly given by the string energy density per unit length, $GU \ll 1$ (in Planck units), which is also the typical energy scale at which these objects are formed, eventually redshifted by warped extra-dimension for the so-called cosmic superstrings [5–8]. Although the theory of cosmological perturbations can be applied to defects [9], predicting string induced anisotropies in the cosmic microwave background (CMB) is challenging. As opposed to the perturbations of inflationary origin, which are generated once and for all in the early universe, active sources require the complete knowledge of their evolution at all times, from their formation until today [10–14].

For these reasons, cosmological analyses often rely on analytical, or semianalytical defect models [15–25] which may not be accurate enough in view of the incoming flow of high precision CMB data, such as those from the Planck satellite and the other suborbital experiments [26–29]. The theoretical understanding of cosmic string evolution in a Friedmann-Lemaître-Robertson-Walker (FLRW) universe is still an active field of research which has led to the development of various theoretical models [30–40] and numerical simulations, the latter having the advantage of incorporating all the defect dynamics [41–52]. However,

within simulations, the dynamical range remains limited such that one has to extrapolate numerical results over orders of magnitude by means of their scale invariant properties. The CMB temperature and polarization angular power spectra have been derived for local strings only within the Abelian Higgs model [53–55]. As simulations do have only one free parameter that is GU , they provide a robust correspondence between string tension and CMB amplitude. From current data, Ref. [56] reports the two-sigma confidence limit $GU < 4.2 \times 10^{-7}$, whereas semi-analytical methods find bounds ranging from 10^{-9} to 10^{-6} [57–60].

Among other signatures, non-Gaussianities are unavoidable consequences of the presence of cosmic strings (see Refs. [61,62] for a review). The determination of the power spectrum, i.e. the two points function, is not easy and the situation is even worse for any higher n -point function. A way around this is to include photons inside a string simulation to produce a realization of the expected CMB temperature anisotropies. In that respect, the resulting map contains all the statistical content, non-Gaussianities included. This method has originally been introduced for Nambu-Goto strings in Ref. [63] and revived in Ref. [64] to create a collection of statistically independent small angle CMB maps. As shown by Hindmarsh, Stebbins, and Veeraraghavan, the small angle limit happens to be very convenient as the perturbed photon propagation equations, namely, the string induced integrated Sachs-Wolfe (ISW) effect [65,66], reduces to a more tractable two-dimensional problem [67,68]. Those maps have been shown to be accurate as they correctly reproduce the small

*christophe.ringeval@uclouvain.be

†bouchet@iap.fr

scale power spectrum of Abelian strings [55] as well as the analytically expected one-point [69–71] and higher n -point functions [72–74]. Although flat sky maps are adequate to devise new string-oriented searches in small scale CMB data [75–77], current searches for non-Gaussianities are mainly driven by the primordial type and based on full sky optimized estimators [78–81] (see Ref. [82] for a review).

In this paper, we generalize the method used in Ref. [64] and go beyond the flat sky approximation to generate a full sky CMB map induced by Nambu-Goto strings. The most unequivocal signature from strings are the temperature discontinuities they induce, which are naturally most striking at small scales; our efforts thus have been to achieve a high resolution over the complete sky. In a hierarchical equal area isolatitude pixelization of the sky, we have been able to maintain an angular resolution of $\theta_{\text{res}} = 0.85'$, i.e. using the publicly available HEALpix code [83], our map has $N_{\text{side}} = 4096$, i.e. 2×10^8 pixels. As detailed in the following, our method includes all string effects from the last scattering surface until today, but does not include the Doppler contributions induced by the strings into the plasma prior to recombination. As a result, our map represents the ISW contribution from strings, which is dominant at small scales but underestimates the signal on intermediate length scales. Including the Doppler effects requires the addition of matter in the simulations, an approach which has been implemented in Refs. [84,85] and recently used to generate a full sky map in Ref. [86]. As discussed in that reference, the computing resources required to include matter severely limit the achievable resolution to $14'$ ($N_{\text{side}} = 256$, with 800 000 pixels). In that respect, our map is complementary to the one of Ref. [86] while extending the domain of applicability of existing small angle maps [57]. In particular, we recover the “turn-over” in the spectrum observed around $\ell \simeq 200$ in Ref. [86], which was cut by the small field of view of the flat sky maps.

The paper is organized as follows. In Sec. II, we briefly recap the characteristics of our numerical simulations of cosmic string networks and describe the ray tracing method used to compute the full sky map. The map itself is presented in Sec. III and compared with the small angle maps in the applicable limit. We also compute the angular power spectrum and conclude in the last section.

II. METHOD

A. All sky string ISW

Denoting by $X^\mu(\tau, \sigma)$ the string embedding functions, in the transverse temporal gauge,¹ up to a dipole term, the integrated Sachs-Wolfe contribution sourced by the Nambu-Goto stress tensor reads [68]

$$\Theta(\hat{n}) = -4GU \int_{X_{\text{rc}}^{\alpha}} \mathbf{u} \cdot \frac{X\hat{n} - \mathbf{X}}{(X\hat{n} - \mathbf{X})^2} \epsilon d\sigma, \quad (1)$$

where $\Theta(\hat{n})$ stands for the relative photon temperature shifts ($\Theta \equiv \Delta T/T$) in the observation direction \hat{n} . The integral is performed over all string position vectors $\mathbf{X} = \{X^i\}$ intercepting our past light cone, the invariant string length element being $d\ell = \epsilon d\sigma$ with $\epsilon^2 \equiv \dot{X}^2 / (1 - \dot{X}^2)$. The string dynamical effects are encoded in

$$\mathbf{u} = \dot{X} - \frac{(\hat{n} \cdot \dot{X}) \cdot \dot{X}}{1 + \hat{n} \cdot \dot{X}}, \quad (2)$$

where the “acute accent” and the “dot” denote differentiation with respect to the world sheet coordinates σ and τ , respectively. The small angle and flat sky approximations consists in taking the limit $X\hat{n} \rightarrow \mathbf{X}$ which assumes that the observation direction matches with the string location and that all photon trajectories are parallel [57,63,67]. Let us notice that Eq. (1) cannot be applied to a straight static string, but such a situation never occurs for the realistic string configurations studied in the following [68,87].

In the following, we use the all sky expression of Eq. (1) to compute the induced temperature anisotropies $\Theta(\hat{n})$ in each of the wanted 2×10^8 pixelized directions. Equation (1) shows that, in each direction, one has to sum up the contribution of *all* string segments $d\ell$ intercepting our past light cone since the last scattering surface and determine, for each of them, \dot{X} and \dot{X} . Although one string lying behind the observer does not contribute more than a few percent to the overall signal, it is impossible to artificially cut it without adding spurious discontinuities in the map, which would dangerously mimic real string patterns. As discussed below, we have filled the comoving volume between today and the last scattering surface with a few thousand Nambu-Goto numerical simulations in FLRW space-time. Typically, hundreds of millions of string segments intercept on our past light cone, and each of them has to be included in Eq. (1) to get the overall signal for one pixel. One can immediately understand the computing challenge to obtain a full sky map as the total number of expected iterations roughly sums up to 10^{16} .

B. Nambu-Goto string simulations

In order to get a realistic string configuration between the last scattering surface and today, we have followed Refs. [63,64] and stacked FLRW string simulations using an improved version of the Bennett and Bouchet Nambu-Goto cosmic string code [43,48]. The runs have the same characteristics as those used in Ref. [64] and, in particular, we include only the loops having a size larger than a time-dependent cutoff. The reason is that loops smaller than this cutoff have a distribution which is known to be contaminated by relaxation effects from the numerical initial conditions. As explained in Ref. [64], the cutoff

¹ $\dot{X} \cdot \dot{X} = 0$, $X^0 = \eta = \tau$, and η is the conformal time.

is dynamically chosen by monitoring the time evolution of the energy density distribution associated with loops of different sizes. This ensures that we include only loops having an energy density evolving as in scaling, i.e. in $1/t^2$. One may be worried about the deficit due to the missing loops artificially removed by the cutoff. An upper bound of the systematic errors that could be induced by these relaxation effects can be found in that same reference (see Sec. II.D in Ref. [64]). It does not exceed 10% on average and concerns only very small scales. In the following, we recap some of the relevant physical properties underlying our numerical simulations (see Sec. II.B in Ref. [64] for more details). Each simulation allows one to trace the time evolution of a network of cosmic strings in scaling over a cubic comoving volume of typical size

$$L_{\text{sim}} \simeq 30 \frac{1 - \sqrt{\Omega_{\text{rad}}/\Omega_{\text{mat}}}\sqrt{1+z_i}}{h\sqrt{\Omega_{\text{mat}}}\sqrt{1+z_i}} \text{ Gpc}. \quad (3)$$

In this expression, z_i is the redshift at which the simulation is started, h is the reduced Hubble parameter today, and Ω_{mat} , Ω_{rad} are the density parameters of matter and radiation today. Starting at the last scattering surface, $z_i = 1089$, gives a simulation comoving box of $L_{\text{sim}} \simeq 1.7 \text{ Gpc}$,² which corresponds to an angular size of 7.2° . At the same time strings are evolved, we propagate photons along the three spatial directions and record all \hat{X} and \hat{Y} for each string segment intercepting those light cones. Depending on the simulation realization, and its location, this corresponds to typically 10^4 – 10^5 projected string segments. One run is limited in time, as we use periodic boundary conditions, and ends after a 30-fold increase in the expansion factor, i.e. at a redshift $z_e = 36$. As a result, covering the whole sky requires stacking side-by-side many different simulations, all starting at $z_i = 1089$ and ending at $z_e = 36$. The missing redshift range can be dealt exactly in the same manner by stacking another set of runs which start at $z_i = 36$ and end at $z_e = 0.2$. From Eq. (3), we see that the low-redshift simulations have a size of $L_{\text{sim}} \simeq 13 \text{ Gpc}$ such that only a few of them are required to cover the whole comoving volume. Notice that the use of different simulations to fill the comoving space does not induce visible artifacts in the final map. The signal is only sourced by the subset of string segments intercepting the past light cone; the probability of seeing an edge is almost vanishing. Finally, as in Ref. [57], we have skipped the last interval from $z = 0.2$ to $z = 0$ as almost no string intercepts our past light cone in that range.

In the next section, we describe in more detail how we cut and stack the cosmic string simulations.

²In the runs, L_{sim} is computed exactly within the Λ CDM model; whereas, Eq. (3) is an analytical approximation assuming no cosmological constant and $\Omega_{\text{rad}} \ll \Omega_{\text{mat}}$.

C. Stacking simulations with healpix cones

The hierarchical equal area isolatitude pixelization (healpix) of the two-sphere is an efficient method to pixelize the sky which is well-suited to and commonly used for CMB analysis [83]. Our stacking method relies on the voxelization of the three-dimensional ball using cones subtending healpix pixels on its boundaries, i.e. for the two redshifts at which we start and stop the numerical simulations. For the high-redshift contributions, the healpix cones fill the whole spherical volume in between the last scattering surface at $z_i = 1089$ and the two-sphere at $z_e = 36$ (see Fig. 1). The rest of the volume, associated with the low redshift simulations, can be voxelized exactly in the same way but starting on the two-sphere at $z_i = 36$ and ending at $z_e = 0.2$. The actual string dynamics simulations are evolved in cubic comoving boxes in which we take only strings living inside a healpix cone. In order to minimize the number of simulations required, the problem is now reduced to find the largest healpix cone fitting inside a cubic comoving box for all redshifts of interest. Moreover, one has to ensure that the photons intercepting the strings travel towards the observer. As seen in Fig. 1, both requirements can be implemented by adequately rotating the simulation box such that photons face the observer line of sight \hat{n} , and the farthest healpix pixel fits inside the farthest squared face of the simulation box. As we propagate three photon waves in each simulation, one can use the same simulation rotated three times. Keeping only the

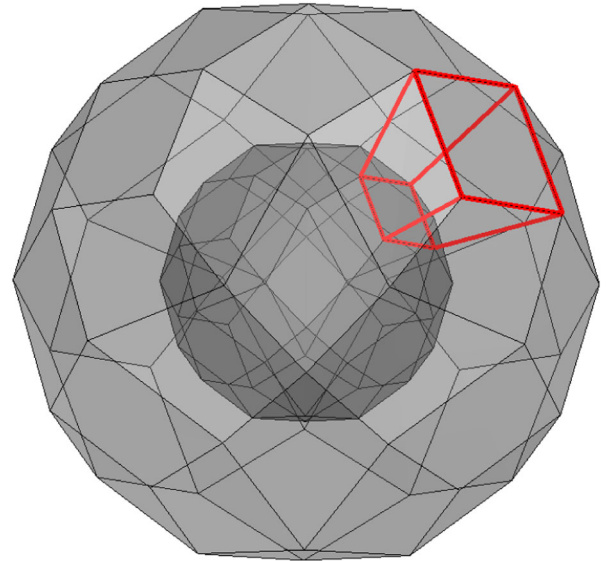


FIG. 1 (color online). Voxelization of the comoving space between the two redshifts at which cosmic string simulations start and stop, here $z_i = 1089$ (outer sphere) and $z_e = 36$ (inner sphere). All strings living in each healpix cone are kept and stacked to fill the whole comoving volume. Our high redshift voxelization scheme uses $N_{\text{side}}^{\text{hz}} = 16$, i.e. requires 3072 string simulations while the low redshift one, starting at $z_i = 36$ and ending now, has $N_{\text{side}}^{\text{lz}} = 1$, i.e. 12 simulations.

strings living inside the healpix cones, one needs to patch them up till the whole comoving volume is filled. For this purpose, we have used the algorithms implemented within the HEALPix library [83].

For the high-redshift contribution, the above requirements are satisfied with a healpix voxelization having $N_{\text{side}}^{\text{hz}} = 16$, i.e. 3072 truncated cones from $z = 1089$ to $z = 36$, therefore calling for 3072 cosmic string runs. As we can use one run three times, we have only performed 1024 independent simulations as described in Sec. II B (and Ref. [57]). Concerning the low-redshift contribution, the simulation volume L_{sim} being much larger, $N_{\text{side}}^{\text{lz}} = 1$ or 12 simulations are enough to cover the volume. Let us emphasize, at this stage, that the above-mentioned HEALpix resolutions only concern the simulation stacking method. In the next section, we discuss how we discretize the CMB sky using another, but more conventional, healpix scheme.

D. Healpix sky

Assuming we have stacked the cosmic string simulations as previously explained, we have at our disposal a realization of all \vec{X} and \vec{X}' lying on our past light cone since the last scattering surface. From Eqs. (1) and (2), the remaining step is to actually perform the integral for each desired value of the observer direction \hat{n} . Choosing the values of \hat{n} has been made by using another healpix pixelization scheme, this time on the simulated sky. A typical Planck-like CMB experiment requiring an angular resolution of $5'$, we have chosen an angular resolution of $0.9'$ to reduce sufficiently the small scale inaccuracies which are present at the subpixel scale. The corresponding healpix resolution is $N_{\text{side}} = 4096$, i.e. a sky map having 2×10^8 pixels.

In the next section, after having briefly exposed how the above computing challenges have been solved, we present the simulated CMB map.

III. STRING SKY MAP

The method we have exposed in the previous section has the advantage to be completely factorizable into two independent numerical problems. The first is to perform string simulations and record only those events intercepting the light cones. The second is to use these events to actually perform the integration of Eq. (1), which gives the final signal $\Theta(\hat{n})$.

A. Computing resources

Performing the one thousand cosmic string runs has required around 300 000 cpu-hour on current x86-64 processors. The needed memory and disk space resources remaining reasonable, the computations have used local computing resources provided by the Planck-HFI computing centre at the ‘‘Institut d’Astrophysique de Paris’’ and the CP3 cosmo cluster at Louvain University. By the end of

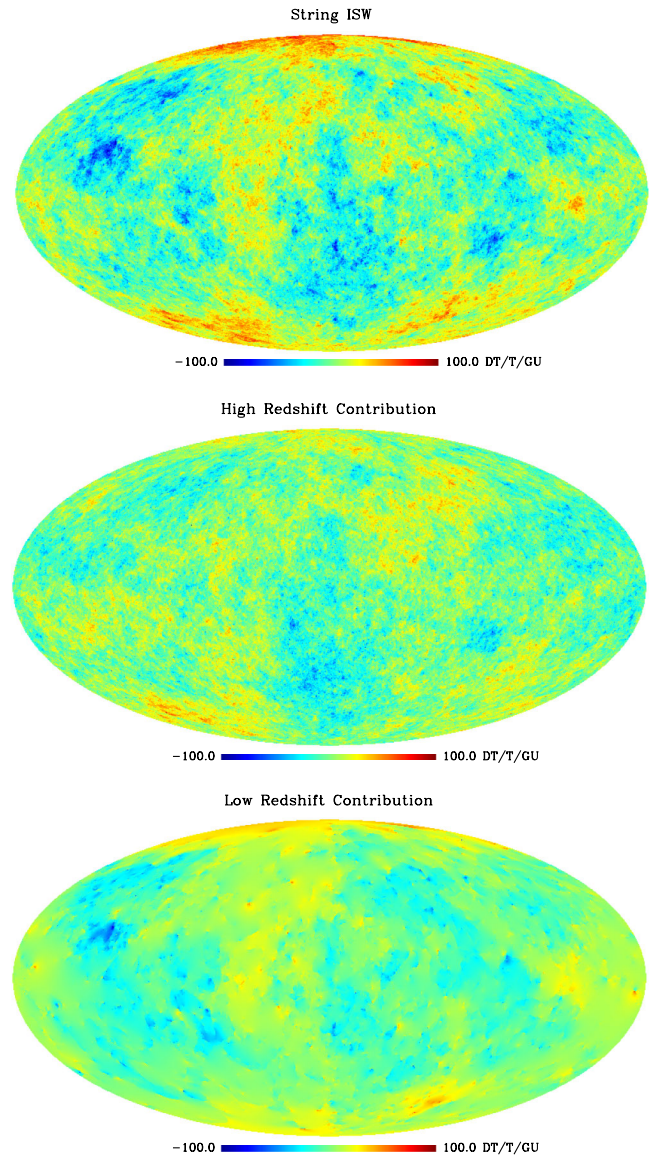


FIG. 2 (color online). All sky CMB map of string induced ISW effect (upper panel) in a Mollweide projection. The two lower maps represent respectively the high redshift contribution (from last scattering to $z = 36$) and the low redshift contribution (from $z = 36$ to now). The color scale indicates the range of Θ/GU fluctuations which, once multiplied by the value of GU and T_{CMB} , would thus be in the tens of μK range for $GU \sim 10^{-6}$.

the runs, the total number of string segments recorded on the light cone account for typically 1 Tb of storage data.

From the light cone data, performing 2×10^8 line of sight integrals over 10^8 string segments [see Eq. (1)] is a serious numerical problem. This part of the code has therefore been parallelized at three levels using the symmetries of the problem.

First, we have used a distributed memory parallelization as implemented in the message passing interface (MPI) to split the string contributions into sub-blocks. From our previous discussion, a natural implementation is an

MPI-parallelization over the healpix cones, which therefore allows different machines to deal with a subset of cones. More intuitively, it means that the final map is obtained by adding up full sky maps, each one sourced by the strings contained in a few healpix cones only. Second, for each of those processes, the computation of the 2×10^8 pixels has been parallelized using the shared memory OpenMP directives. In other words, pixels can be simultaneously computed using all of the available processors inside a single machine. Finally, for each of the above OpenMP threads, we have vectorized the most inner loop, i.e. the discrete version of Eq. (1). Doing this allows one to use simultaneously multiple registers of each processing unit to add up a few string segments at once.

The computing resources have been provided by the National Energy Research Scientific Computing Center (NERSC) at the Lawrence Berkeley National Laboratory.³ The run has been performed on the hopper super-computer using 512 MPI nodes at the first level of parallelization. On each node, we have deployed the OpenMP parallelization over the 24 cores available. Each node is made of two twelve-cores “AMD MagnyCours” cpu’s which supports only a limited amount of vectorization. However, a vectorization over 16 string segments significantly improves cache memory latency and gives a final speed-up of two compared to a pure scalar processing. All in all, the whole computation required 12 000 cores and has been completed after 500 000 cpu-hour.

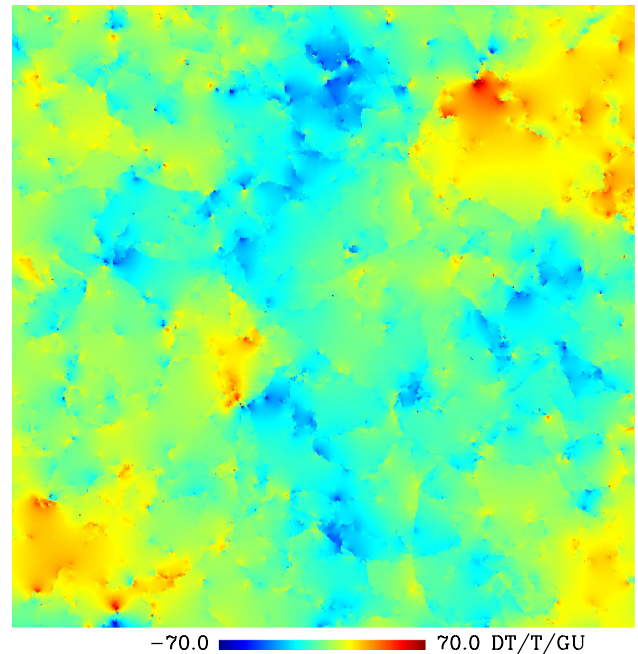
B. Results

In Fig. 2, we have plotted the final map together with the two contributions coming from high and low redshift. As expected, most of the strings are at high redshift, the low redshift contribution showing only a few strings crossing the sky. For this reason, we have not included strings with $z < 0.2$, as almost no strings are present.

At first glance, these maps may look Gaussian, which is because the string patterns essentially show up at small scales while they are averaged on the largest angular scales [86]. In Fig. 3, we have represented a zoom over a 7.2° region in which one recovers the same string discontinuities as previously derived within the flat sky approximation [57]. In order to make the comparison sharper, both the gnomonic projection of our spherical patch and the flat sky map coming from the same string simulation are represented in Fig. 3. Up to some spherical distortions off-center, both maps predict the same structures.

Finally, in Fig. 4, we have plotted the angular power spectrum obtained from the full sky map. In this figure, the dashed curve represents the mean value previously derived using flat sky patches in Ref. [57]. We observe a very small loss of power compared to the flat sky result, which may

Gnomonic projection



Flat sky

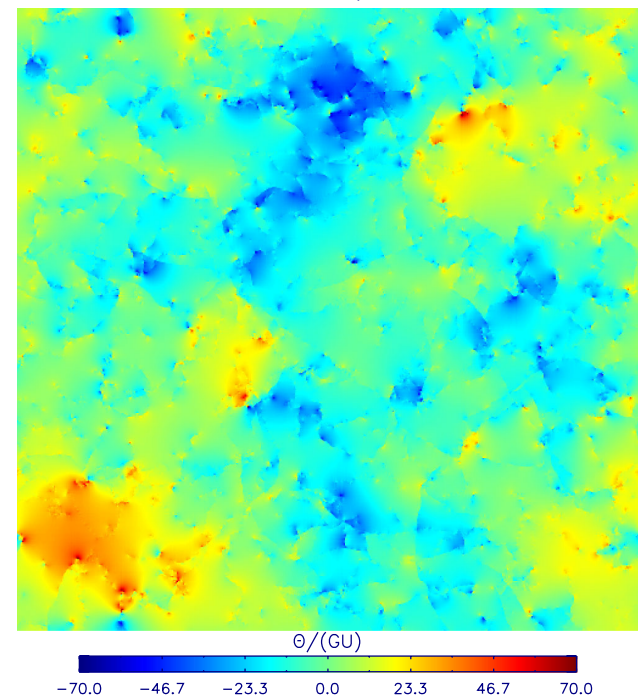


FIG. 3 (color online). Comparison between full sky and flat sky/small angle approximation. The upper panel is a gnomonic projection of a 7.2° patch cut from the high redshift full sky map at the north pole. The lower panel is from Ref. [57] and represents the high redshift flat sky calculation coming from the same string simulation. Both maps exhibit globally the same anisotropy patterns and amplitude. More precisely, there is essentially no difference in the center; whereas, geometrical and amplitude distortions become increasingly apparent towards the edges. This is expected as spherical effects are not included in the flat sky approximation.

³<http://www.nersc.gov>

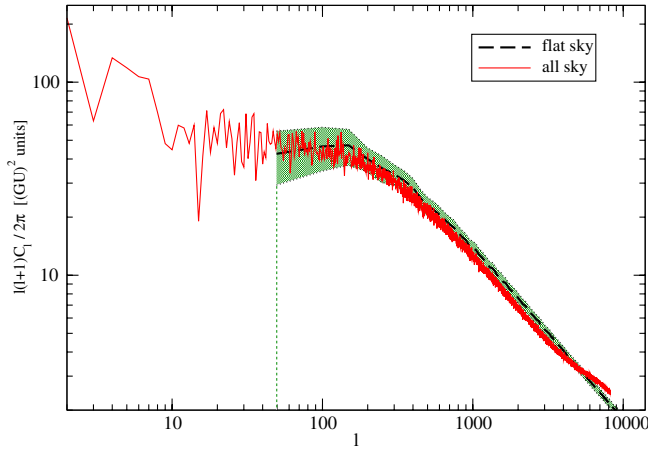


FIG. 4 (color online). Angular power spectrum extracted from the string map of Fig. 2 (solid red curve) compared to the one estimated in Ref. [57], using the small angle and flat sky approximation (dashed black curve). The shaded region represents the one-sigma fluctuations over various string realizations (flat sky).

not be significant as it does not exceed the one-sigma fluctuations expected between various string realizations. However, as Fig. 3 suggests, the flat sky maps are a bit sharper than the spherical ones due to some missing spherical effects and, as such, they may slightly overestimate the signal. This is not surprising as the flat sky maps are derived using the small angle approximated version of Eq. (1) where all scalar products are postulated to be either parallel or null [67]. As our full sky map does not approximate anything, it should contain slightly less power.

Let us also notice that there is some extra power for $\ell > 5000$ associated with the full sky power spectrum. This is a spurious aliasing effect coming from the slow decrease of the power spectrum at small scales combined with our ray tracing method. Each pixel of the map represents the real signal, but only in the centroid direction \hat{n} . This has the effect of including string structures

smaller than the pixel angular resolution thereby aliasing the final map.

In Fig. 4, the power spectrum turns over for $\ell < 200$ as those modes correspond to wavelengths larger than the correlation length at recombination. This property was also observed in the map derived in Ref. [86] but barely visible in the flat sky maps of Ref. [57] due to their small field of view. We see, *a posteriori*, that this effect was, however, indeed present as the dash curve of Fig. 4 flattens at the same location than the full sky spectrum.

IV. CONCLUSION

The main result of this article is the map displayed in Fig. 2 which provides a realization of the all sky CMB temperature anisotropies induced by a network of cosmic strings since the last scattering surface. The challenges underlying this map come from both the requirement of covering the whole sky and an unprecedented angular resolution of 0.85 minute of arc, associated with a HEALpix resolution of $N_{\text{side}} = 4096$. However, our map includes only the ISW string contribution. This is the dominant signal at small scales, but it misses the Doppler effects around the intermediate multipoles. As those effects have been computed in Ref. [86], at the expense of having a poor resolution, it will be interesting to investigate whether both results can be combined to obtain a fully accurate representation of the stringy sky over the full range of observable scales.

ACKNOWLEDGMENTS

This research used resources of the National Energy Research Scientific Computing Center, which is supported by the Office of Science of the U.S. Department of Energy under Contract No. DE-AC02-05CH11231. This work is also partially supported by the Wallonia-Brussels Federation Grant No. ARC 11/15-040 and ESA under the Belgian Federal PRODEX Program No. 4000103071.

-
- [1] T. W. B. Kibble, *J. Phys. A* **9**, 1387 (1976).
 - [2] U.-L. Pen, U. Seljak, and N. Turok, *Phys. Rev. Lett.* **79**, 1611 (1997).
 - [3] R. Durrer and M. Kunz, *Phys. Rev. D* **57**, R3199 (1998).
 - [4] R. Durrer and Z.-H. Zhou, *Phys. Rev. D* **53**, 5394 (1996).
 - [5] E. J. Copeland, R. C. Myers, and J. Polchinski, *J. High Energy Phys.* **06** (2004) 013.
 - [6] A.-C. Davis and T. Kibble, *Contemp. Phys.* **46**, 313 (2005).
 - [7] M. Sakellariadou, *Nucl. Phys. B, Proc. Suppl.* **192**, 68 (2009).
 - [8] E. J. Copeland and T. W. B. Kibble, *Proc. R. Soc. A* **466**, 623 (2010).
 - [9] R. Durrer, M. Kunz, and A. Melchiorri, *Phys. Rep.* **364**, 1 (2002).
 - [10] U.-L. Pen, D. N. Spergel, and N. Turok, *Phys. Rev. D* **49**, 692 (1994).
 - [11] J. Magueijo, A. J. Albrecht, P. Ferreira, and D. Coulson, *Phys. Rev. D* **54**, 3727 (1996).
 - [12] J. Magueijo, A. Albrecht, D. Coulson, and P. Ferreira, *Phys. Rev. Lett.* **76**, 2617 (1996).
 - [13] A. Achucarro, J. Borrill, and A. R. Liddle, *Phys. Rev. Lett.* **82**, 3742 (1999).
 - [14] C. Contaldi, M. Hindmarsh, and J. Magueijo, *Phys. Rev. Lett.* **82**, 679 (1999).

- [15] L. Pogosian and T. Vachaspati, *Phys. Rev. D* **60**, 083504 (1999).
- [16] A. Gangui, L. Pogosian, and S. Winitzki, *Phys. Rev. D* **64**, 043001 (2001).
- [17] X. Siemens, J. Creighton, I. Maor, S.R. Majumder, K. Cannon, and J. Read, *Phys. Rev. D* **73**, 105001 (2006).
- [18] E. Jeong and G.F. Smoot, *Astrophys. J.* **661**, L1 (2007).
- [19] L. Pogosian and M. Wyman, *Phys. Rev. D* **77**, 083509 (2008).
- [20] M. S. Pshirkov and A. V. Tuntsov, *Phys. Rev. D* **81**, 083519 (2010).
- [21] R.J. Danos and R.H. Brandenberger, *J. Cosmol. Astropart. Phys.* **02** (2010) 033.
- [22] A. V. Tuntsov and M. S. Pshirkov, *Phys. Rev. D* **81**, 063523 (2010).
- [23] R.J. Danos, R.H. Brandenberger, and G. Holder, *Phys. Rev. D* **82**, 023513 (2010).
- [24] P. Demorest, R. Ferdman, M. Gonzalez, D. Nice, S. Ransom *et al.*, [arXiv:1201.6641](https://arxiv.org/abs/1201.6641).
- [25] K. Kamada, Y. Miyamoto, and J. Yokoyama, [arXiv:1204.3237](https://arxiv.org/abs/1204.3237).
- [26] K.M. Huffenberger and U. Seljak, *New Astron. Rev.* **10**, 491 (2005).
- [27] J. Ruhl *et al.*, *Proc. SPIE* 5498, 11 (2004).
- [28] R. Barker *et al.* (AMI Collaboration), *Mon. Not. R. Astron. Soc.* **369**, L1 (2006).
- [29] P.A.R. Ade, N. Aghanim, M. Arnaud, M. Ashdown, J. Aumont, C. Baccigalupi, M. Baker, A. Balbi, A. J. Banday *et al.* (Planck Collaboration), *Astron. Astrophys.* **536**, 16464 (2011).
- [30] D. Austin, E. J. Copeland, and T. W. B. Kibble, *Phys. Rev. D* **48**, 5594 (1993).
- [31] E. J. Copeland, T. W. B. Kibble, and D. A. Steer, *Phys. Rev. D* **58**, 043508 (1998).
- [32] C. J. A. P. Martins and E. P. S. Shellard, *Phys. Rev. D* **65**, 043514 (2002).
- [33] J. Polchinski and J. V. Rocha, *Phys. Rev. D* **74**, 083504 (2006).
- [34] F. Dubath, J. Polchinski, and J. V. Rocha, *Phys. Rev. D* **77**, 123528 (2008).
- [35] J. V. Rocha, *Phys. Rev. Lett.* **100**, 071601 (2008).
- [36] E. J. Copeland and T. W. B. Kibble, *Phys. Rev. D* **80**, 123523 (2009).
- [37] C. Martins, *Phys. Rev. D* **80**, 083527 (2009).
- [38] L. Lorenz, C. Ringeval, and M. Sakellariadou, *J. Cosmol. Astropart. Phys.* **10** (2010) 003.
- [39] A. Poursidou, A. Avgoustidis, E. Copeland, L. Pogosian, and D. Steer, *Phys. Rev. D* **83**, 063525 (2011).
- [40] A. Avgoustidis, E. Copeland, A. Moss, L. Pogosian, A. Poursidou, and D. A. Steer, *Phys. Rev. Lett.* **107**, 121301 (2011).
- [41] D. P. Bennett and F. R. Bouchet, *Phys. Rev. Lett.* **63**, 2776 (1989).
- [42] A. Albrecht and N. Turok, *Phys. Rev. D* **40**, 973 (1989).
- [43] D. P. Bennett and F. R. Bouchet, *Phys. Rev. D* **41**, 2408 (1990).
- [44] B. Allen and P. Shellard, *Phys. Rev. Lett.* **64**, 119 (1990).
- [45] G. Vincent, N. D. Antunes, and M. Hindmarsh, *Phys. Rev. Lett.* **80**, 2277 (1998).
- [46] J. N. Moore, E. P. S. Shellard, and C. J. A. P. Martins, *Phys. Rev. D* **65**, 023503 (2001).
- [47] J.-H. P. Wu, P. P. Avelino, E. P. S. Shellard, and B. Allen, *Int. J. Mod. Phys. D* **11**, 61 (2002).
- [48] C. Ringeval, M. Sakellariadou, and F. Bouchet, *J. Cosmol. Astropart. Phys.* **02** (2007) 023.
- [49] V. Vanchurin, K. Olum, and A. Vilenkin, *Phys. Rev. D* **72**, 063514 (2005).
- [50] K. D. Olum and V. Vanchurin, *Phys. Rev. D* **75**, 063521 (2007).
- [51] C. J. A. P. Martins and E. P. S. Shellard, *Phys. Rev. D* **73**, 043515 (2006).
- [52] J. J. Blanco-Pillado, K. D. Olum, and B. Shlaer, *Phys. Rev. D* **83**, 083514 (2011).
- [53] N. Bevis, M. Hindmarsh, M. Kunz, and J. Urrestilla, *Phys. Rev. D* **75**, 065015 (2007).
- [54] N. Bevis, M. Hindmarsh, M. Kunz, and J. Urrestilla, *Phys. Rev. D* **76**, 043005 (2007).
- [55] N. Bevis, M. Hindmarsh, M. Kunz, and J. Urrestilla, *Phys. Rev. D* **82**, 065004 (2010).
- [56] J. Urrestilla, N. Bevis, M. Hindmarsh, and M. Kunz, *J. Cosmol. Astropart. Phys.* **12** (2011) 021.
- [57] A. A. Fraisse, *J. Cosmol. Astropart. Phys.* **03** (2007) 008.
- [58] M. Sadegh Movahed and S. Khosravi, *J. Cosmol. Astropart. Phys.* **03** (2011) 012.
- [59] R. Battye and A. Moss, *Phys. Rev. D* **82**, 023521 (2010).
- [60] C. Dvorkin, M. Wyman, and W. Hu, *Phys. Rev. D* **84**, 123519 (2011).
- [61] C. Ringeval, *Adv. Astron.* **2010**, 380507 (2010).
- [62] M. Hindmarsh, *Prog. Theor. Phys. Suppl.* **190**, 197 (2011).
- [63] F. R. Bouchet, D. P. Bennett, and A. Stebbins, *Nature (London)* **335**, 410 (1988).
- [64] A. A. Fraisse, C. Ringeval, D. N. Spergel, and F. R. Bouchet, *Phys. Rev. D* **78**, 043535 (2008).
- [65] J. R. Gott, III, *Astrophys. J.* **288**, 422 (1985).
- [66] N. Kaiser and A. Stebbins, *Nature (London)* **310**, 391 (1984).
- [67] M. Hindmarsh, *Astrophys. J.* **431**, 534 (1994).
- [68] A. Stebbins and S. Veeraraghavan, *Phys. Rev. D* **51**, 1465 (1995).
- [69] K. Takahashi A. Narukob, Y. Sendoudab, D. Yamauchib, C.-M. Yoo, and M. Sasaki, *J. Cosmol. Astropart. Phys.* **10** (2009) 003.
- [70] D. Yamauchi, K. Takahashi, Y. Sendouda, C.-M. Yoo, and M. Sasaki, *Phys. Rev. D* **82**, 063518 (2010).
- [71] D. Yamauchi, Y. Sendouda, C.-M. Yoo, K. Takahashi, A. Naruko, and M. Sasaki, *J. Cosmol. Astropart. Phys.* **05** (2010) 033.
- [72] M. Hindmarsh, C. Ringeval, and T. Suyama, *Phys. Rev. D* **80**, 083501 (2009).
- [73] M. Hindmarsh, C. Ringeval, and T. Suyama, *Phys. Rev. D* **81**, 063505 (2010).
- [74] D. M. Regan and E. P. S. Shellard, *Phys. Rev. D* **82**, 063527 (2010).
- [75] D. K. Hammond, Y. Wiaux, and P. Vandergeynst, *Mon. Not. R. Astron. Soc.* **398**, 1317 (2009).
- [76] M. D. Niemack *et al.*, *Proc. SPIE* 7741, 77411S (2010).
- [77] J. Dunkley *et al.*, *Astrophys. J.* **739**, 52 (2011).
- [78] M. Liguori, E. Sefusatti, J. Fergusson, and E. Shellard, *Adv. Astron.* **2010**, 980523 (2010).

- [79] D. Regan, E. Shellard, and J. Fergusson, *Phys. Rev. D* **82**, 023520 (2010).
- [80] J. Fergusson, M. Liguori, and E. Shellard, *Phys. Rev. D* **82**, 023502 (2010).
- [81] A. Curto, E. Martinez-Gonzalez, R. Barreiro, and M. Hobson, [arXiv:1105.6106](https://arxiv.org/abs/1105.6106) (Mon. Not. R. Astron. Soc. [to be published]).
- [82] D. Huterer, S. Shandera, and E. Komatsu, *Adv. Astron.* **2010**, 697147 (2010).
- [83] K. Gorski, E. Hivon, A. Banday, B. Wandelt, F. Hansen, M. Reinecke, and M. Bartelmann, *Astrophys. J.* **622**, 759 (2005).
- [84] M. Landriau and E. Shellard, *Phys. Rev. D* **67**, 103512 (2003).
- [85] M. Landriau and E. Shellard, *Phys. Rev. D* **69**, 023003 (2004).
- [86] M. Landriau and E. Shellard, *Phys. Rev. D* **83**, 043516 (2011).
- [87] S. Veeraraghavan and A. Stebbins, *Astrophys. J. Lett.* **395**, L55 (1992).